NeuroImage 127 (2016) 215–226

Contents lists available at ScienceDirect

NeuroImage

journal homepage: www.elsevier.com/locate/ynimg

Acceptance of evidence-supported hypotheses generates a stronger signal from an underlying functionally-connected network

J.C. Whitman [a,*], Y. Takane [b,c], T.P.L. Cheung [d,e], A. Moiseev [d], U. Ribary [d,f], L.M. Ward [a,d], T.S. Woodward [d,g]

[a] Department of Psychology, University of British Columbia, 2136 West Mall, Vancouver, BC V6T 1Z4, Canada
[b] Department of Psychology, University of Victoria, Canada
[c] Department of Psychology, McGill University, Canada
[d] Behavioral & Cognitive Neuroscience Institute, Canada
[e] School of Engineering, Simon Fraser University, Canada
[f] Department of Psychology, Simon Fraser University, Canada
[g] Department of Psychiatry, University of British Columbia, Canada

ARTICLE INFO

Article history:
Received 25 July 2015
Accepted 7 December 2015
Available online 15 December 2015

Keywords:
Hypothesis judgment
Decision-making
Functional connectivity
MEG
fMRI
CPCA

ABSTRACT

Choosing one's preferred hypothesis requires multiple brain regions to work in concert as a functionally connected network. We predicted that a stronger network signal would underlie cognitive coherence between a hypothesis and the available evidence. In order to identify such functionally connected networks in magnetoencephalography (MEG) data, we first localized the generators of changes in oscillatory power within three frequency bands, namely alpha (7–13 Hz), beta (18–24 Hz), and theta (3–7 Hz), with a spatial resolution of 5 mm and temporal resolution of 50 ms. We then used principal component analysis (PCA) to identify functionally connected networks reflecting co-varying post-stimulus changes in power. As predicted, PCA revealed a functionally connected network with a stronger signal when the evidence supported accepting the hypothesis being judged. This difference was driven by beta-band power decreases in the left dorsolateral prefrontal cortex (DLPFC), ventromedial prefrontal cortex (VMPFC), posterior cingulate cortex (PCC), and midline occipital cortex.

Introduction

One cognitive function fundamental to human thought is choosing whether to accept a hypothesis. This underlies interpreting what you perceive, deciding how to act, and forming beliefs. When you judge a hypothesis, you will form a mental representation of how it relates to the available evidence. That mental representation or *gestalt* (Köhler, 1929; Metzger, 2006) should be more coherent and stable if the evidence 'fits' — in other words, if it supports the hypothesis being judged. This is demonstrated in how people are biased against evidence disconfirming their current beliefs (Buchy et al., 2007; Woodward et al., 2007), biased toward interpreting new evidence as being consistent with currently preferred interpretations (Whitman and Woodward, 2012), and generally biased toward gathering and perceiving evidence confirming their current opinions (Nickerson, 1998; Sanbonmatsu et al., 1998; Wason, 1960). The common theme across these findings is a cognitive bias favoring mental representations of evidence–hypothesis matches. We propose that this bias stems from a fundamental organizational principle of how the brain operates: namely, by forming connections between groups of neurons. Connections formed dynamically between the large sets of neurons underlying the mental representation of one concept (i.e. a hypothesis) and the sets of neurons underlying the mental representations of other concepts (i.e. items of evidence) would be easily supported by the brain's mechanisms for functional connectivity. Hence, we predicted that a match between a hypothesis being judged and the available evidence – in other words, greater cognitive coherence – should correspond to a stronger signal from at least one underlying functionally connected brain network.

In order to ask whether functionally connected network signals grew stronger in response to evidence–hypothesis matches, we analyzed the activity of brain networks while participants performed a hypothesis judgment task. Brain activity was recorded via magnetoencephalography (MEG). MEG measures a real-time signal, similar to that of the more widely used electroencephalography (EEG), but orthogonal to it and less subject to spatial distortions (Herdman and Cheyne, 2009). In the hypothesis judgment task, the available evidence either supported accepting the hypothesis being judged (referred to hereon as the *focal* hypothesis), or supported rejecting it in favor of an alternative hypothesis. The focal and alternative hypotheses each corresponded to a lake containing a mixture of black and white fish (see Fig. 1). On each trial, a single black or white fish appeared in a downstream lake. Participants had to judge the probability that it had migrated there from the focal lake rather than the alternative lake. They responded by using the buttons on a response box (right-handed)

* Corresponding author. Fax: +1 604 822 6923.
E-mail address: jenwhitman@gmail.com (J.C. Whitman).

http://dx.doi.org/10.1016/j.neuroimage.2015.12.011
1053-8119/

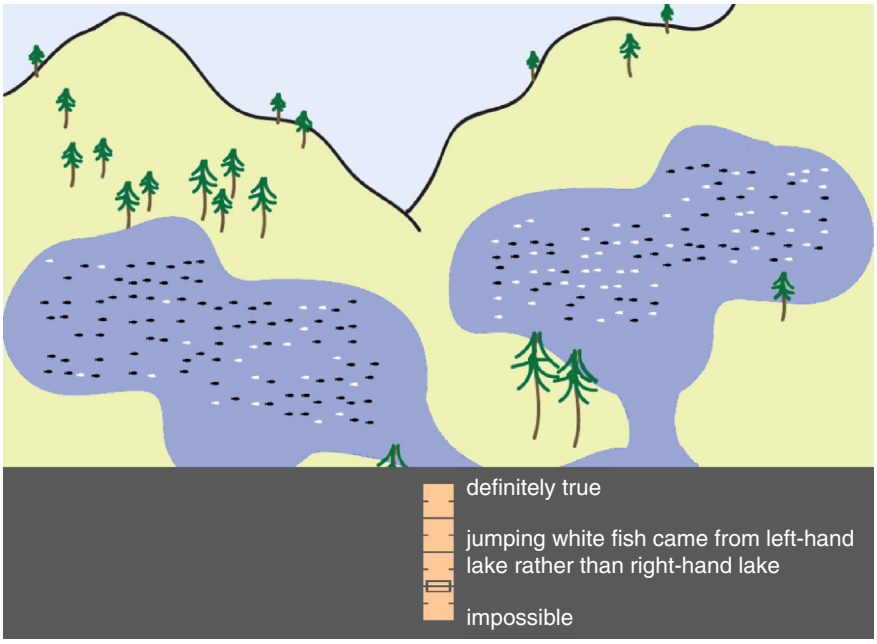

Fig. 1. The hypothesis judgment task performed by participants. At the beginning of each trial, the participants were presented with two upstream lakes, each containing a mixture of black and white fish, and a third, empty downstream lake. A single fish, randomly selected to be either black or white, jumped within the downstream lake (jump duration was 140 ms). A Likert scale on a black background then appeared, with the text "definitely true" at the top end and "impossible" at the bottom end. In the example depicted here, the question next to the Likert scale asks the participant to rate their agreement with the statement that the "jumping *white* fish came from the *left*-hand lake rather than the *right*-hand lake". In that example, the left-hand lake is the *focal* hypothesis, while the right-hand lake is the *alternative* hypothesis. The participant thus correctly rejects the focal hypothesis. The color of the jumping fish (black or white) and the location of the lake corresponding to the focal hypothesis (left-hand vs. right-hand lake) were randomized across trials. Throughout each inter-trial interval, the Likert scale and black background disappeared, and each of the lakes was empty.

to move a cursor up or down a rating scale. This was an adaptation of a paradigm described in our previously published work (Whitman, Metzak, Lavigne, and Woodward, 2013). Our goal was to identify at least one functionally connected network of brain regions displaying a stronger signal when the evidence matched the focal hypothesis, and the combined mental representation was thus more coherent.

In order to characterize functional networks underlying this task with high spatial and temporal detail, we used a beamformer algorithm to create whole-brain images of changes in oscillatory power. Use of beamformer algorithms to localize the cortical generators of oscillatory signals in MEG data can produce brain maps with a level of spatial detail similar to those seen at the cluster level in functional magnetic resonance imaging (fMRI). We were able to produce one image for each successive 50 ms post-stimulus interval by using a sliding window to average across temporally overlapping estimates of oscillatory power. This was done separately for three frequency ranges of interest, known as the alpha (7–13 Hz), beta (18 to 24 Hz), and theta (3–7 Hz) frequency bands (Engel and Fries, 2010; Kelly et al., 2006; Wu et al., 2007), and separately for each experimental condition of interest: whether evidence supported or refuted the focal hypothesis. Each beamformed image represented activity combined across trials within a given condition. We then assessed how changes in the power of cortical oscillations covaried over time between brain regions and frequency bands. To this purpose, we used principal component analysis (PCA) to identify, in an efficient and data-driven manner, the dominant brain networks defined by shared time courses of post-stimulus changes in oscillatory power. PCA analyzes a matrix of covariances or correlations between variable values (in this case spectral power in a specific frequency band at each voxel) into orthogonal components, with each component accounting for part of the pattern of covariances (Jolliffe, 1986).

We expected the brain networks involved in performing the hypothesis judgment task to include regions of the dorsal attention, vision, and frontoparietal control networks (Yeo et al., 2011) with strong contributions from parietal and lateral occipital cortices, as was found in our previous fMRI study of hypothesis judgment (Whitman et al., 2013a). We also predicted that the left dorsolateral prefrontal cortex (DLPFC), reported to be involved in perceptual decision-making (Heekeren et al., 2004; Heekeren et al., 2006; Kim and Shadlen, 1999), might figure prominently. While the left DLPFC did not figure prominently in our previous fMRI study, its role may be more evident in the MEG data, which involve real-time measures with a much higher temporal resolution than fMRI.

The examination of oscillations in several distinct frequency bands may also reveal effects not detectable by fMRI. The power of cortical oscillations in several characteristic frequency bands is known to vary as a function of several cognitive factors. There is an extensive literature on how the power of alpha-band oscillations over parietal and occipital regions varies with spatial attention (Kelly et al., 2006; Rihs et al., 2007; Sauseng et al., 2005a; Worden et al., 2000), and literature on the role of theta-band oscillations in central executive functions, working memory, and task switching (Sauseng et al., 2010; Sauseng et al., 2005b; Schack et al., 2005; Wu et al., 2007). Changes in beta-band power in motor cortex contralateral to a hand being moved are associated with motor activity (Pfurtscheller et al., 1996; Pfurtscheller et al., 2003). Beta-band oscillations in multiple brain regions, including prefrontal and parietal cortices, are associated with insightful problem-solving and perceptual decision-making (Donner et al., 2009; Sheth et al., 2009; Siegel et al., 2011). We predicted that a functionally connected brain network, involving changes in oscillatory power covarying across at least some of the brain regions specified above, and potentially also covarying across frequency bands, would exhibit a stronger signal when the evidence supported accepting the focal hypothesis.

Materials and methods

Ethics approval for all experiments reported here was obtained from the UBC Clinical Research Ethics Board and the Vancouver Coastal Health Research Institute. All participants provided written informed consent.

Participants

Twenty healthy adults (10 female, 10 male) with a mean age of 25.9 years (SD = 5.9) volunteered in the experiment. Participants were reimbursed $10 per hour plus transportation expenses. All participants were right-handed. Participants were recruited via posters on the UBC campus and in community centers in the greater Vancouver area, and via postings on online bulletin boards. Ethical approval was provided by the University of British Columbia Clinical Research Ethics Board. Participants were excluded from participating if they could not safely undergo an MRI scan, if they had experienced any head injuries resulting in loss of consciousness for more than 20 min, if they suffered from epilepsy, encephalitis, or meningitis, of if they or an immediate family member suffered from a psychotic illness (e.g. schizophrenia or bipolar disorder).

Task

Task summary

In order to characterize, with high spatial and temporal detail, functional brain networks sensitive to evidence–hypothesis matches, we collected both MEG and fMRI data while participants performed a hypothesis judgment task. As stated above, this required participants to judge the probability that a given fish had migrated from one lake, corresponding to the *focal* hypothesis, rather than another lake, corresponding to the *alternative* hypothesis. The task performed in the MEG study was identical to that in the fMRI study for which the methods are published elsewhere (Whitman et al., 2013a), with the following exceptions. The number of trials per condition was increased by a factor of two, the participants were allowed a maximum of 5 s to respond, and the average ITI (inter-trial interval) was shortened so that it varied randomly between 1500 ms and 2500 ms. There were two experimental runs of 980 s, each consisting of four blocks of trials. Each of the four blocks per run started with 10 s during which the task instructions were presented. A 20 s rest break was presented between the 2nd and 3rd blocks of each run. There were also 24 s of rest at the end of each run. Each of the analyses reported in this paper included the data from four experimental conditions of interest stemming from two factors. The first was whether the evidence supported accepting or rejecting the focal hypothesis. The second factor corresponded to how much the focal and alternative hypotheses differed in terms of evidence strength. While manipulating the strength of evidence helped to keep participants engaged in the task, it was not of primary theoretical interest. In the later stages of data analysis we collapsed across this second factor, and focused only on whether the evidence supported accepting or rejecting the focal hypothesis.

Task details

The following task details are also described in the previously published fMRI paper (Whitman et al., 2013a). The current paper focuses on whether the available evidence supports or refutes the focal hypothesis during a hypothesis judgment task. We focused on this contrast in our analysis of the MEG data because it was a significant effect in the previously analyzed fMRI data. However, the overall design of the study also included an evidence assessment task, in which there was no need to compare hypotheses, but the visual stimuli presented and the motor activity involved in responding matched the hypothesis judgment task. The hypothesis judgment task (requiring comparison of the focal and alternative hypotheses) and the evidence assessment task were performed in separate, alternating blocks. This is described in more detail below.

On each trial of the task, the participants were presented with a scene depicting three lakes, two of which were upstream from the third (see Fig. 1). At the beginning of each trial, an animated series of images was displayed, depicting a single fish, either black or white, breaking the surface, jumping along an inverted U-shaped path (parabolic) for 140 ms, then disappearing again below the surface. We will refer to the color of this jumping fish as the relevant color. The color of this fish was also specified throughout the remaining duration of the trial within the question adjacent to the rating scale. This ensured that the participants would be aware of the current relevant color even if they had not seen the fish jump. The populations of 100 fish in each of the two upstream lakes then became visible. Aside from the jumping fish, no other fish were ever visible in the downstream lake. The positions of the black and white fish within each lake were randomized over trials, so that any two trials with identical ratios of black to white fish would not be identical in appearance. On hypothesis comparison trials, the participants were told that any fish appearing in the downstream lake originated in either the left-hand upstream lake or the right-hand upstream lake. They were required to rate the probability that the jumping fish came from one particular lake (the focal lake) rather than the alternative lake. The assignment of the left-hand and right-hand lakes as focal and alternative hypotheses was randomized across trials. On the evidence assessment trials, the participants reported the percentage of fish of the relevant color in both lakes together.

In the fMRI task, each trial allowed a maximum of 6 s for the participant to make a rating. As 6 s was more than sufficient time in the sample of participants who performed the fMRI task first, we designed the MEG task to allow a maximum of 5 s for ratings to be made. All responses were made by moving a slider up or down a vertical response scale using button presses on a LUMItouch fiber-optic response device (Lightwave Medical, Vancouver, British Columbia, Canada). The entire scale was 160 pixels in length. All responses were made with the dominant (right) hand. The two outer response buttons served to move the cursor either up or down 10 pixels (the index finger moved the cursor down), while the two inner response buttons served to move the cursor either up or down 2 pixels (the middle finger moved the cursor down).

The evidence assessment and hypothesis comparison tasks were performed in alternating blocks of 14 trials each, with 4 blocks per functional run. There were 7 sub-conditions within the hypothesis comparison task, corresponding to different percentages of fish of the relevant color in the focal and alternative lakes. If the percentage was 20% in the focal lake, it was either 20% or 50% in the alternative lake. If it was 50% in the focal lake, it was 20%, 50%, or 80% in the alternative lake. If it was 80% in the focal lake, it was either 50% or 80% in the alternative lake. Thus, the 7 sub-conditions matched the structure of a Likert scale: the evidence strongly favored accepting the focal hypothesis (50% focal vs. 20% alternative), weakly favored it (80% focal vs. 50% alternative), was neutral (80% vs. 80%, 50% vs. 50%, or 20% vs. 20%), weakly favored rejecting the focal hypothesis (50% focal vs. 80% alternative), or strongly favored rejecting the focal hypothesis (20% focal vs. 50% alternative). There were also 7 sub-conditions in the evidence assessment task that used the same visual displays, but these required the participants to rate the percentage of fish of the relevant color in both lakes combined.

In the fMRI task, for each of those 14 sub-conditions, there were 2 trials per run with an inter-trial interval (ITI) of 2 s and 2 trials per run with an ITI of 8 s. During the ITI, three empty lakes were displayed, i.e. without fish or a response scale. The average ITI (inter-trial interval) in the MEG task was shortened so that it varied randomly between 1500 ms and 2500 ms. Halfway through each experimental run of the fMRI task, a 30-second rest break occurred, during which the words "Take a 30 s break" were displayed on a dark gray screen. In the MEG task, this was a 20-second break.

The number of trials per sub-condition was doubled from 8 in the fMRI task to 16 in the MEG task. As the MEG analysis reported here averages across the two sub-conditions with strong and weak support for accepting the focal hypothesis and the two sub-conditions with strong and weak support for the alternative, the two main conditions in the analysis of MEG data reported in the current paper (Accept Focal vs. Reject Focal) each represent a total of 32 trials.

fMRI image acquisition

Imaging was performed at the University of British Columbia's MRI Research Centre on a Philips Achieva 3.0 Tesla scanner with Quasar Dual gradients (with peak strength of 80 mT/m and maximum slew rate of 200 T/m/s). The participant's head was firmly secured using a custom head holder. Functional image volumes were collected with T2*-weighted gradient echo spin pulse sequences (TR = 2000 ms, TE = 30 ms, flip angle 90°, 36 slices, 3 mm thick, 1 mm gap, sense factor 2, matrix is 80 × 80 reconstructed at 128, FOV = 240 mm × 240.0 mm × 143 mm, measured voxel is 3 mm × 3 mm × 3 mm, actual bandwidth per pixel is 53.6 Hz) effectively covering the whole brain (143 mm axial extent). Each participant completed one structural scan and two functional runs of 370 scans each.

MEG data acquisition and coregistration with structural MRIs

MEG data were recorded at 1200 Hz by a 151-channel CTF system inside a magnetically shielded room. Electromagnetic coils were placed at three fiducial points on the participant's head; the nasion and the left and right pre-auricular points. These were energized before and after each recording session in order to measure head position. Data were recorded in supine position and padding was placed around the head to minimize movement. The locations of the fiducial coils and the participants' head shapes were recorded using a 3-D digitizer (Polhemus Isotrak). Locations of these fiducial coils were also photographed at very close range, so that markers could be placed in the same locations during the MRI scans. The location of the MEG sensors was co-registered to the brain anatomy by matching the locations of the fiducial markers in the MEG data to the markers on the structural MRI scans using MRIViewer software. Visual stimuli were projected onto a screen and then reflected from a mirror above the participant. Responses were made using a Lumitouch response box, always with the right (dominant) hand. We also used a regression algorithm to remove ocular artifacts arising from blinks and eye movements from the ongoing data, as is explained in more detail in Appendix A. While such ocular artifacts are unlikely to bias estimates of oscillatory power in specific frequency bands, we felt that removing them would still aid our analysis by reducing the overall amount of noise in the data. Anatomical and functional MRI scans were acquired from the same participants on separate days from the MEG scans. Details of the structural and functional MRI scans are described in previously published work (Whitman et al., 2013a).

Analyses of oscillatory power and beamformer source localization

Using FieldTrip software (Oostenveld et al., 2011), we used a DPSS multitaper to estimate oscillatory power within three frequency bands: alpha (7–13 Hz), beta (18–24 Hz), and theta (3–7 Hz). These frequencies of interest were selected partly on the basis of previous literature and partly on the basis of visual inspection of time–frequency plots of the signal time-locked to stimulus onset at individual MEG sensors. In order to estimate the locations of the brain networks generating the MEG signal, and to be able to compare the spatial patterns of those networks to those of the fMRI networks, we used a DICS beamformer algorithm (Gross et al., 2001). Each participant's structural MRI scan was used to constrain the solution. We localized oscillations to grid points spaced 5 mm apart. The images output by the beamformer were spatially normalized and smoothed in SPM5 software so that they were in the same space as the fMRI data. This allowed the use of the fMRI results as spatial constraints to be applied to the MEG data in our multimodal analysis. In order to minimize the computer memory needed, we also used a gray matter mask (the average brain template available as part of the MRIcron software package) to exclude any voxels/grid points in our fMRI/MEG data that did not represent gray matter. We also modified the mask to exclude any subcortical gray matters such as the thalamus and brainstem. These deep sources would be unlikely generators of the MEG signal measured outside the head, as the strength of magnetic fields decreases with the inverse square of the distance. As a result, we included 10,036 grid points from each beamformed image. While the term grid points is standard in source localization of MEG data, we will refer to the grid points hereon as voxels for the sake of consistency with the fMRI data, particularly for the analysis in which we merge our MEG and fMRI results.

Each beamformed image represented activity combined across trials within a given experimental condition, participant, run, and frequency band of interest. Within each of four experimental conditions and three frequency bands of interest, we obtained a whole-brain estimate of oscillatory power for every 50 ms post-stimulus interval. As trials were 5000 ms in total duration, this resulted in a separate brain image for each of 100 post-stimulus time bins. In order to accomplish this, we first created beamformed images corresponding to much wider time windows. This was necessary because an accurate estimate of oscillatory power requires a wide enough time window to fit several cycles at that frequency. Specifically, for the theta frequency band, we produced one image corresponding to the interval from 0 to 1000 ms post-stimulus, one image corresponding to the interval from 50 to 1050 ms post-stimulus, etc. In order to estimate the time courses of activity with more temporal detail, we then applied a sliding average to the temporally overlapping brain images output by the beamformer algorithm. This is analogous to the sliding average approach commonly used in time–frequency plots at individual MEG sensors or EEG electrodes (Delorme and Makeig, 2004). In order to ensure that each 50 ms time bin between 0 and 5000 ms post-stimulus represented an average of the same number of overlapping time windows, we produced beamformed images ranging from 1000 ms pre-stimulus to 5950 ms post-stimulus. Within the faster alpha and beta frequency bands, we used time windows 750 ms rather than 1000 ms in width. The computational demands of applying such a sliding average approach to whole-brain images, rather than data at individual sensors, were met via the high-performance computing facilities provided by the Compute Canada consortium — specifically, the WestGrid facilities.

Identification of functional networks

The analyses of oscillatory power and source localization described above were performed separately for each participant ($N = 20$) and each run (two per participant). We then combined all of the beamformed images into one large data matrix with 16,000 rows, corresponding to 100 post-stimulus time bins × 4 conditions × 2 runs per participant × 20 participants. There were 30,108 columns in the data matrix, corresponding to 10,036 voxels × 3 frequency bands. In order to ensure that the results of our PCA analysis were not dominated by any single participant or run, we standardized the data so that, within each column, the set of 400 rows corresponding to a single run had a mean of 0 and a standard deviation of 1. Following standardization, we performed PCA on the full data matrix. Each principal component identified corresponded to one functionally connected network. We used singular value decomposition — specifically, the svd function as implemented in Matlab,

$$\left[U\ D\ V'\right] = \mathrm{svd}(Z)$$

where Z is the data matrix (described above) to be submitted to svd, U, the matrix of left singular vectors, provides the component scores for each component extracted (corresponding to post-stimulus time courses), V, the right singular vector, contains the patterns in the loadings for each component extracted (corresponding to spatial patterns in brain images), and D is a diagonal matrix containing the singular values used to compute how much variance was accounted for by each component.

In our multimodal analysis of functional networks, we combined the MEG data with fMRI data from the same participants performing the same task. To accomplish this, we first regressed our MEG data onto column constraints representing the spatial patterns of the fMRI networks. We then performed PCA on the predicted scores from that regression. The general application of this constrained principal component analysis (CPCA) is described in previously published work (Hunter and Takane, 2002). In the current study, the MEG data matrix, referred to as *Z*, contained 16,000 rows and 30,108 columns. The matrix of constraints to be applied to the columns of *Z* will be referred to hereon as *H*. This *H* matrix allowed us to assess how well the MEG data matched the spatial patterns defined by the fMRI networks — specifically, a study-specific version of the default mode network (DMN) and a frontoparietal–occipital network which we refer to here as the FPO network, identified in our previously published study (Whitman et al., 2013a). The *H* matrix had 30,108 rows, corresponding to the 30,108 columns of *Z*. In order to assess how well the MEG data in our 3 frequency bands of interest matched our 2 fMRI networks, we needed 6 separate contrasts. These formed the 6 columns of *H*. The first column of *H* involved the FPO image from rows 1 to 10,036, then zeros in rows 10,037 to 30,108. The second column of *H* involved the FPO image from rows 10,037 to 20,072, and zeros from rows 1 to 10,036 and rows 20,073 to 30,108. The third column of *H* involved the FPO image from rows 20,073 to 30,108, and zeros from rows 1 to 20,073. The fourth, fifth, and sixth columns of *H* followed an analogous pattern, except that the DMN image was used in place of the FPO image. In the regression step, the *Z* matrix is regressed onto the *H* matrix to produce producing a matrix of predicted scores (*BH′*) and a matrix of residuals (*E*).

$$Z = BH' + E$$

After regressing *Z* onto *H*, we performed singular value decomposition on the predicted scores (*BH′*) from that regression, as specified in the general application of CPCA (Hunter and Takane, 2002). In the current study, our PCA suggested extracting three components, as is described in the Results section. Regressing the right singular vectors of the resulting principal components onto the *H* matrix allowed us to form *H*-predictor weights specifying how the spatial pattern of each MEG network matched that of our fMRI networks. This was assessed separately for each of the three frequency bands because the *H* matrix contained a separate pair of spatial predictors for each frequency. Thus, we had 18 predictor weights in total, corresponding to 3 principal components × 6 contrasts from the *H* matrix.

Results and discussion

Behavioral data

Ratings made on the Likert scale showed that, as expected, the participants judged the focal hypothesis to be more probable on trials in which the evidence supported accepting it than on trials in which the evidence supported rejecting it, $t(19) = 5.72$, $p < .001$. The average rating placed the cursor at a location corresponding to 64.1% of the height of the rating scale ($SD = 9.6$) in the Accept-Focal condition and 38.6% ($SD = 11.8$) in the Reject-Focal condition. The time spent making ratings did not differ significantly, $t(19) = 1.70$, *ns*, between the Accept-Focal condition ($M = 1.1$ s, $SD = .3$) and the Reject-Focal condition ($M = 1.0$ s, $SD = .4$). However, participants did initiate their responses earlier, $t(19) = 3.09$, $p < .01$, in the Accept-Focal condition ($M = 3.5$ s, $SD = .4$) than in the Reject-Focal condition ($M = 3.7$ s, $SD = .5$).

Oscillatory networks underlying hypothesis judgment

Our principal component analysis (PCA) of the MEG data identified three distributed brain networks involved in the performance of the hypothesis judgment task, corresponding to the three largest principal components. Collectively, these accounted for 68% of the variance in our data matrix of post-stimulus changes in oscillatory power. The first principal component accounted for 32%, the second principal component accounted for 24%, and the third principal component accounted for 12% of the variance. These are depicted in Figs. 2–4. The spatial pattern of each network is depicted by the *loadings* of each voxel and frequency band combination onto each principal component.

The post-stimulus time course of each network is depicted by the *component scores* for that principal component. The higher the component score in each time bin, the stronger the influence of the spatial pattern for that network. The time course of component scores thus depicts the time course of increasing or decreasing strength of the signal from that functionally connected network. As component scores provided a separate time course for each participant and each condition of interest, we were able to perform inferential statistics testing for differences between conditions in the strength of the signal from the functionally connected network during the post-stimulus interval. Within each condition, the component scores at time bins 2 through 100 were expressed as a difference from the score at time bin 1, so that the Accept and Reject conditions (evidence coherent vs. not coherent with the focal hypothesis) were equal at the time of stimulus onset. For each principal component, we performed a 2 × 99 ANOVA (analysis of variance) with factors of decision (Accept vs. Reject Focal Hypothesis) and time bin.

Network 1: Alpha-band and beta-band oscillations in visual areas

The network corresponding to the first principal component was dominated by parietal and lateral occipital decreases in alpha- and beta-band power (see Fig. 2). Strong responses from these parietal and lateral occipital clusters are often seen in fMRI paradigms with large visual displays (Lavigne et al., 2015; Whitman et al., 2013b). In the ANOVA performed on component scores, we found a significant main effect of time bin, $F(98,1862) = 34.38$, $p < .001$, $\eta^2 = .64$. Neither the main effect of decision, $F(1,19) = 3.26$, *nsig*, nor the interaction of decision with time bin, $F(98,1862) = .52$, *nsig*, was significant. These results reflect how the post-stimulus time course deviated substantially from zero, but the time courses of the Accept and Reject conditions did not diverge significantly from each other. These findings suggest that this parietal–occipital network was involved in aspects of the task independent from deciding whether to accept or reject the focal hypothesis — namely, analyzing the large visual scene used to present the evidence and monitoring the position of the slider on the rating scale while a response was made.

Network 2: Theta-band oscillations spanning bilateral parietal cortex and SMA

The network corresponding to the second principal component (Fig. 3) was dominated by bilateral parietal, pre-central and post-central increases in theta-band power. In the ANOVA performed on component scores, we found a significant main effect of time bin, $F(98,1862) = 67.73$, $p < .001$, $\eta^2 = .78$, no significant main effect of decision, $F(1,19) = .40$, *nsig*, and a significant interaction of decision with time bin, $F(98,1862) = 1.29$, $p < .05$, $\eta^2 = .06$. As can be seen in Fig. 3, this interaction is driven by a stronger signal from the functionally connected network in the Accept condition in the middle of the post-stimulus period, and a weaker signal at the end. These differences were quite small relative to the magnitude of the time course's overall deviation from zero (the extent to which the time course, averaged across conditions, deviates from a flat line).

Network 3: Beta-band oscillations in left DLPFC, midline occipital cortex, PCC and VMPFC

The network corresponding to the third principal component (Fig. 4) was dominated by increases in alpha-band power in a midline region spanning the precuneus, posterior cingulate cortex (PCC), central

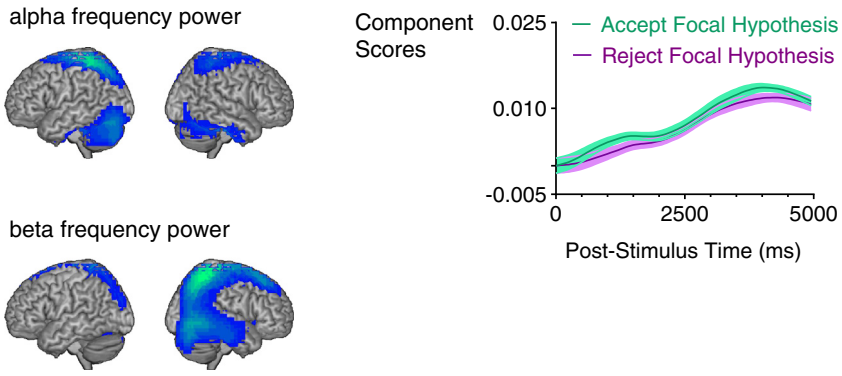

Fig. 2. The functional brain network corresponding to principal component 1 extracted from the MEG data. The thresholds used for inclusion in the rendered brain images were not significance thresholds. Rather, they were selected to depict the dominant spatial patterns defining each network as clearly as possible. The voxels with the most extreme 30% of loadings for this component are depicted. The spatial pattern is dominated by decreases (blue and green in brain images) in alpha-band and beta-band power. In the plotted post-stimulus time courses for the strength of each network signal, error bars (colors around trend lines in graphs) represent the standard error of the mean.

sulcus, and supplementary motor area (SMA), and by decreases in beta-band power in the PCC, midline occipital cortex, ventromedial prefrontal cortex (VMPFC), and the left dorsolateral prefrontal cortex (left DLPFC). In the ANOVA performed on component scores, we found a significant main effect of time bin, $F(98,1862) = 2.99$, $p < .001$, $\eta^2 = .14$, no significant main effect of decision, $F(1,19) = .31$, *nsig*, and a significant interaction of decision with time bin, $F(98,1862) = 1.44$, $p < .01$, $\eta^2 = .07$. As can be seen in Fig. 4, the difference between the Accept and Reject conditions is substantial relative to the magnitude of the time course's overall deviation from zero. This is consistent with our prediction that at least one functionally connected network would exhibit a stronger signal when the available evidence was coherent with the focal hypothesis. In order to better understand this network, we performed follow-up analyses to describe the contributions of individual brain regions and frequency bands.

Region-specific and frequency-specific effects of evidence–hypothesis matches

In order to determine how much changes in alpha-band and beta-band power within each distinct region of the third principal component contributed to the difference in time course between conditions, we created a mask for each cluster (formed from adjacent voxels). There was one mask for the midline region of the central sulcus where component loadings were strong in the alpha-band, and four masks for regions where component loadings were strong in the beta-band: the left DLPFC, VMPFC, PCC, and midline occipital cortex. We then examined the time course of changes in power in the alpha or beta frequency bands averaged across the voxels within each cluster. As can be seen in Fig. 5, when the evidence supported accepting the focal hypothesis there was a much stronger decrease in beta-band power in the left DLPFC, VMPFC, PCC, and midline occipital cortex. Within each cluster, there was a significant main effect of time bin, a significant interaction of decision with time bin (all p-values $< 10^{-12}$), and no main effect of decision (all p-values $> .28$). Details of these ANOVAs are displayed in Table 1. To better distinguish between the contributions of the five clusters examined, we also performed planned contrasts of the interaction of decision with the linear trend of time bin. As is also shown in Table 1, this was significant for changes in beta-band power in the midline occipital cluster, the PCC, the VMPFC, and the left DLPFC. The same contrast was not significant for changes in alpha-band power in the midline central sulcus. In sum, the responsiveness of regions within this network to cognitive coherence (leading to decisions to accept the focal hypothesis) seemed to be driven by activity in the beta-band rather than by activity in the alpha-band.

Multimodal MEG–fMRI analysis to confirm spatial patterns of MEG networks

In order to explicitly assess the relationship between the oscillatory networks described above and the networks that can be identified in the fMRI signal, we conducted a multimodal analysis combining MEG and fMRI data. Each participant included in this analysis performed the task in both an fMRI scanner and a MEG sensor array, on separate days. The two fMRI networks involved in this task are reported in previously published work (Whitman et al., 2013a). Briefly, the strongest network involved bilateral parietal and lateral occipital cortices and the dorsal anterior cingulate cortex. As was reported previously, the signal from that functionally connected network identified in the fMRI data was stronger when evidence supported accepting the focal hypothesis. The second-strongest network involved stimulus-induced decreases in activation in the PCC and VMPFC, and showed no difference between conditions in the fMRI study (Whitman et al., 2013a). These two networks from the fMRI study were used as spatial constraints to be applied to the MEG data. This was done separately for each of our 3

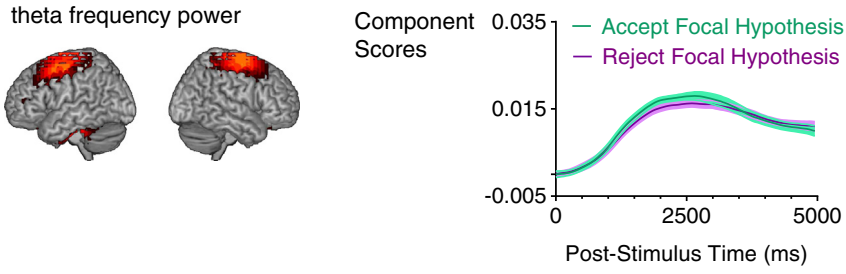

Fig. 3. The functional brain network corresponding to principal component 2 extracted from the MEG data. The thresholds used for inclusion in the rendered brain images were not significance thresholds. Rather, they were selected to depict the dominant spatial patterns defining each network as clearly as possible. The voxels with the most extreme 10% of loadings are depicted. The spatial pattern is dominated by increases (red and yellow in brain images) in theta-band power. In the plotted post-stimulus time courses for the strength of each network signal, error bars (colors around trend lines in graphs) represent the standard error of the mean.

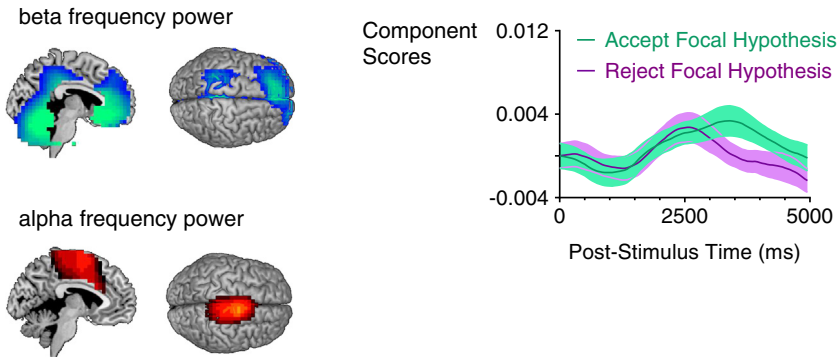

Fig. 4. The functional brain network corresponding to principal component 3 extracted from the MEG data. The thresholds used for inclusion in the rendered brain images were not significance thresholds. Rather, they were selected to depict the dominant spatial patterns defining each network as clearly as possible. The voxels with the most extreme 10% of loadings are depicted. The spatial pattern is dominated by increases (red and yellow in brain images) in alpha-band power and decreases (blue and green in brain images) in beta-band power. In the plotted post-stimulus time courses for the strength of each network signal, error bars (colors around trend lines in graphs) represent the standard error of the mean.

frequency bands of interest. The resultant 6 predictors, corresponding to 2 fMRI networks × 3 MEG frequency bands, were used in a multivariate multiple regression, as is described in more detail in the Materials and Methods section above. This allowed us to constrain the analysis of time courses of changes in oscillatory power to the brain networks identified from the fMRI data, thereby combining the temporal precision and detailed frequency spectrum provided by MEG with the spatial precision of fMRI.

We then performed PCA on this matrixof MEG data with variance constrained to that predictable from the spatial patterns of the fMRI data. We identified 3 networks, depicted in Figs. 6–8. Collectively, these accounted for 98% of the variance in the MEG data predictable from the spatial patterns specified by the fMRI networks. The first principal component accounted for 47%, the second principal component accounted for 34%, and the third principal component accounted for 17% of the variance. The time courses of these three networks closely matched the time courses of the three networks identified in the unimodal MEG analysis, and followed the same relative ordering in terms of the percentage of variance accounted for by descending components.

The spatial pattern of each network from our multimodal analysis is provided with reference to the spatial predictors defined by the fMRI networks. Within each of our three networks from the multimodal analysis, and each of the three frequency bands of interest, we have two predictor weights. One predictor weight indexes the fit to the spatial pattern of the fronto-parietal–occipital network (referred to hereon as the FPO network). The other indexes the fit to the spatial pattern of the default-mode network, or DMN (Buckner et al., 2008). Thus, we

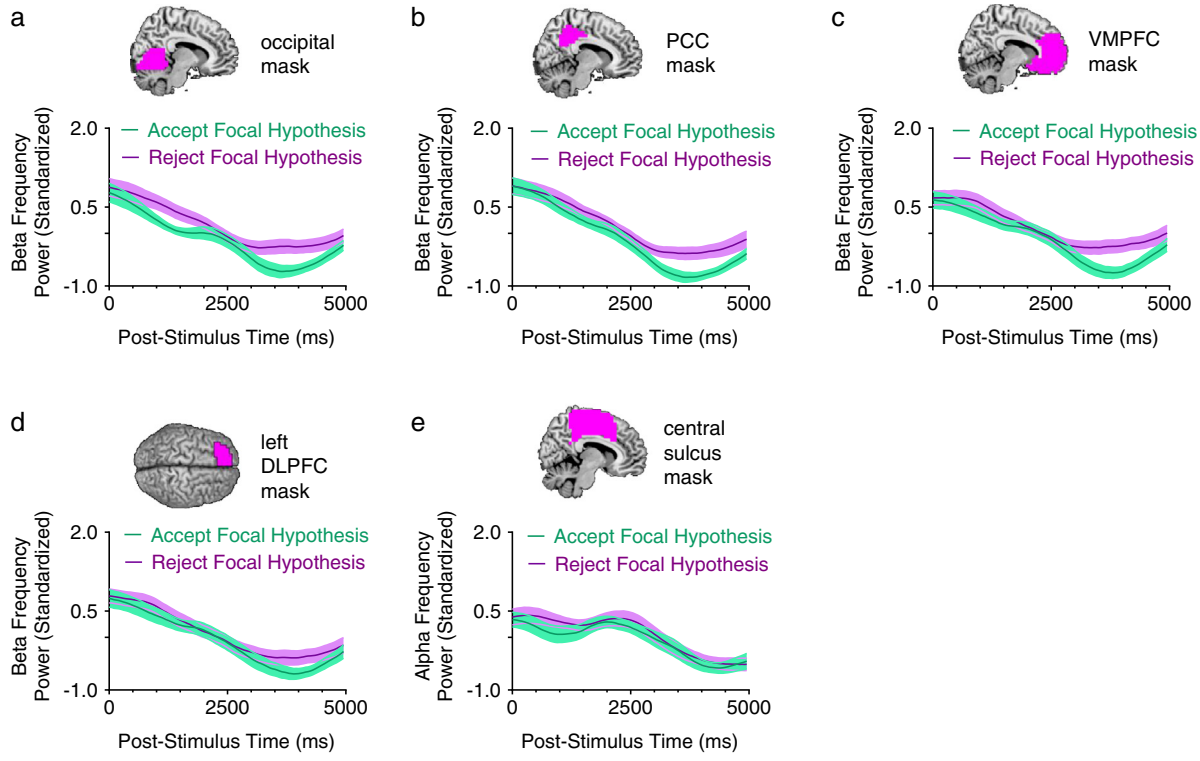

Fig. 5. Post-stimulus time courses of changes in oscillatory power in the beta (18–24 Hz) and alpha (5–7 Hz) frequency bands within individual clusters identified from the third principal component extracted from the MEG data (these are the clusters displayed in Fig. 4). Individual cluster masks (purple color in brain images) and post-stimulus time courses are for a) midline occipital cortex (beta-band power), b) posterior cingulate cortex (beta-band power), c) ventromedial prefrontal cortex (beta-band power), d) left dorsolateral prefrontal cortex (beta-band power), and e) midline central sulcus (alpha-band power).

Table 1
ANOVAs on post-stimulus changes in alpha and beta power averaged across voxels within each of the five clusters of the network corresponding to the third principal component (see Figs. 4 and 5).

	Time bin main effect			Decision main effect			Interaction			Decision × linear trend of time bin		
Cluster	F	p	η^2	F	p	η^2	F	p	η^2	F	p	η^2
Midline occipital (beta)	12.40	10^{-13}	.39	1.21	.286	.06	30.09	$<10^{-16}$	.61	13.90	.001	.42
PCC (beta)	20.95	10^{-13}	.52	1.20	.288	.06	35.73	$<10^{-16}$	.65	10.86	.004	.36
VMPFC (beta)	11.27	10^{-13}	.37	1.12	.304	.06	18.35	10^{-13}	.49	8.08	.010	.30
Left DLPFC (beta)	11.30	10^{-13}	.37	.42	.526	.02	24.07	10^{-13}	.56	8.29	.010	.30
Midline central sulcus (alpha)	6.22	10^{-13}	.25	.01	.942	.00	13.49	10^{-13}	.42	.65	.430	.03

Note. For each ANOVA in this table, the degrees of freedom for the main effect of decision were $F(1,19)$. For the main effect of time bin and the interaction of decision with time bin, they were $F(98,1862)$. For the post-hoc contrast for the interaction of decision with the linear trend of time bin, they were $F(1,19)$.

have six predictor weights per network identified in the multimodal analysis.

For the first principal component of the multimodal analysis (see Fig. 6), the strongest predictor weights are negative for the FPO network in the alpha and beta frequency bands. This is consistent with the decreases in alpha and beta powers in parietal and lateral occipital regions in the first principal component of the unimodal MEG analysis (see Fig. 2). In the ANOVA performed on component scores, we found a significant main effect of time bin, $F(98,1862) = 32.24$, $p < .001$, $\eta^2 = .63$. Neither the main effect of decision, $F(1,19) = 3.25$, *nsig*, nor the interaction of decision with time bin, $F(98,1862) = .53$, *nsig*, was significant.

In the second principal component of the multimodal analysis (see Fig. 7), the strongest predictor weight is positive for the FPO network in the theta-band. This is consistent with the increase in theta-band power in a cluster spanning bilateral parietal cortex and SMA in the second principal component of the unimodal MEG analysis (see Fig. 3). In the ANOVA performed on component scores, we found a significant main effect of time bin, $F(98,1862) = 69.46$, $p < .001$, $\eta^2 = .79$, no significant main effect of decision, $F(1,19) = .48$, *nsig*, and a significant interaction of decision with time bin, $F(98,1862) = 1.31$, $p < .05$, $\eta^2 = .06$.

In the third principal component of the multimodal analysis (see Fig. 8), the strongest predictor weights are positive in the alpha-band and negative in the beta-band for both the FPO network and the DMN. This is consistent with the decreased beta-band power, in the third principal component of the unimodal MEG analysis (see Fig. 4), both in DMN regions such as the PCC and VMPFC and FPO network regions such as the left DLPFC. It is also consistent with the increased alpha-band power in a midline region spanning the PCC and precuneus (DMN regions) and the central sulcus and supplemental motor area (FPO network regions). In the ANOVA performed on component scores, we found a significant main effect of time bin, $F(98,1862) = 2.67$, $p < .001$, $\eta^2 = .12$, no significant main effect of decision, $F(1,19) = .31$, *nsig*, and a significant interaction of decision with time bin, $F(98,1862) = 1.43$, $p < .01$, $\eta^2 = .07$.

In summary, the first principal component of the multimodal MEG–fMRI analysis corresponds closely to the first principal component of the unimodal MEG analysis, both in terms of the spatial pattern and the post-stimulus time course. Similarly, the second principal component of the multimodal analysis corresponds to the second principal component of the unimodal analysis, and the third principal component of the multimodal analysis corresponds to the third principal component of the unimodal analysis. The similarities of the post-stimulus time courses are evident when one compares Fig. 6 with Fig. 2, Fig. 7 with Fig. 3, and Fig. 8 with Fig. 4. The results of the corresponding ANOVAs are also highly similar, though not identical. This correspondence suggests that the estimates of the locations of the generators of the MEG signals correspond to the patterns evident in the more spatially precise fMRI data. This indicates that we succeeded in combining the spatial precision of fMRI with the temporal precision and spectral detail (alpha, beta, and theta frequency bands) of MEG.

Conclusions

The goal of this study was to investigate the neural signature underlying cognitive coherence between a hypothesis being judged and the available evidence. We expected cognitive coherence to correspond to a stronger signal from an underlying functionally connected network. As predicted, we found a stronger signal, when the evidence was coherent with the focal hypothesis being judged (i.e. when the evidence supported accepting it), from a functionally connected network involving increased alpha-band power in the midline central sulcus, and, perhaps more interestingly, decreased beta-band power in the midline occipital cortex, the PCC, the VMPFC, and the left DLPFC. The involvement of the left DLPFC is consistent with previous reports that it plays a role in

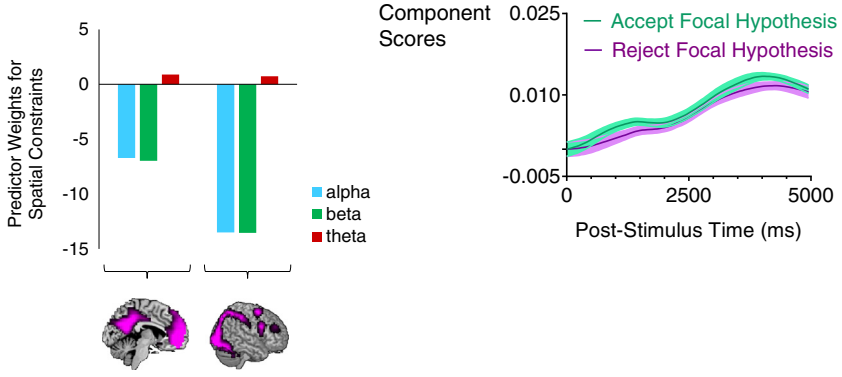

Fig. 6. Principal component 1 of the multimodal MEG–fMRI analysis, dominated by decreased alpha-band and beta-band power in regions of the fronto-parietal–occipital (FPO) network. In plots of the post-stimulus time courses of component scores, error bars (colors around trend lines in graphs at the right) represent the standard error of the mean. Brain images are from the previously published fMRI study and form the spatial constraints applied to the MEG data in the multimodal analysis. The intensity of the purple shading on those brain images represents the strength of the fMRI component loadings (absolute value) for that voxel for that component.

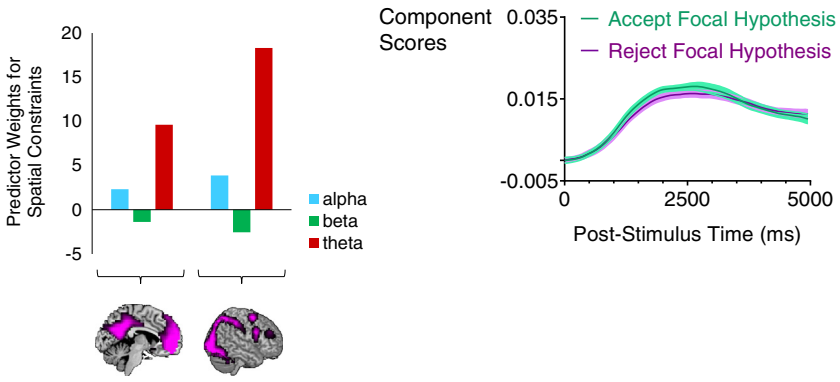

Fig. 7. Principal component 2 of the multimodal MEG–fMRI analysis, dominated by increases in theta-band power in regions of the fronto-parietal–occipital (FPO) network. In plots of the post-stimulus time courses of component scores, error bars (colors around trend lines in graphs at the right) represent the standard error of the mean. Brain images are from the previously published fMRI study and form the spatial constraints applied to the MEG data in the multimodal analysis. The intensity of the purple shading on those brain images represents the strength of the fMRI component loadings (absolute value) for that voxel for that component.

perceptual decision-making (Heekeren et al., 2004; Heekeren et al., 2006; Kim and Shadlen, 1999). In a follow-up analysis, we assessed the contributions of the left DLPFC, VMPFC, PCC, midline occipital cortex, and midline central sulcus separately. The left DLPFC, VMPFC, PCC, and midline occipital cortex each showed a stronger decrease in beta-band power when the evidence supported accepting the focal hypothesis. There was no such difference evident for the increased alpha power in the midline central sulcus. This indicates that the sensitivity of this network to cognitive coherence between the focal hypothesis and the available evidence is driven by beta-band oscillations.

One intriguing aspect of our findings is that two of the brain regions most strongly involved in our effect of interest, namely the ventromedial prefrontal cortex (VMPFC) and posterior cingulate cortex (PCC), are widely associated with mind-wandering or off-task processing in fMRI studies of the default-mode network, or DMN (Buckner et al., 2008; Christoff et al., 2009; Fox et al., 2005). This highlights a flawed assumption often made in the fMRI literature; the assumption that a decrease in the fMRI blood oxygenation signal is evidence of decreased involvement in the cognitive task performed. There is no reason why the extent to which a brain region accurately extracts meaning from incoming information must necessarily be reflected in increased metabolic demands averaged across the whole population of neurons within that region. Rather, meaning extraction often corresponds to how well neural activity is organized into a specific *pattern*. This forms the conceptual foundation for multivariate pattern analysis (MVPA) of fMRI data (Haxby, 2012). Furthermore, in the literature on cortical oscillations, increases and decreases in power are both often considered indicative of task involvement. A decrease in power often corresponds to an increase in spatial attention (Kelly et al., 2006; Rihs et al., 2007; Sauseng et al., 2005a; Worden et al., 2000) or motor activity (Pfurtscheller et al., 1996; Pfurtscheller et al., 2003). In the current study, we have evidence that two regions widely thought to be involved in off-task processing in the fMRI literature, and found to decrease their signal in our fMRI study employing this task, are revealed by MEG data to actually play a key role in task performance. Thus, the findings from our analysis of cortical oscillations indicate a need to rethink the fMRI-based interpretations of the role of the 'default-mode network' (Buckner et al., 2008; Fox et al., 2005; Fox et al., 2009).

The findings of the current study exemplify some of the advantages of measuring cortical oscillations to study the brain networks underlying hypothesis judgment. These networks must necessarily be able to change configuration rapidly and flexibly, and cortical oscillations certainly display such flexibility. MEG is well-suited to detecting such rapid changes, as it provides real-time measures of activity with millisecond resolution. On the other hand, the signals associated with distinct cognitive events tend to merge in fMRI, as it relies on changes in blood oxygenation peaking 5 to 6 s after a stimulus is displayed.

Another advantage of studying cortical oscillations is that distinct frequencies can potentially be linked to distinct neural networks. For example, 40 Hz gamma oscillations coordinate activity between the CA1 and CA3 regions of the hippocampus, while 60 Hz gamma oscillations synchronize activity between the CA1 region and medial entorhinal cortex (Belluscio et al., 2012; Colgin et al., 2009; Whitman, Ward, & Woodward, 2013). On a broader scale, 10 Hz alpha oscillations have been shown to synchronize activity between parietal and lateral occipital cortices (Doesburg et al., 2009a) and 5 Hz theta oscillations

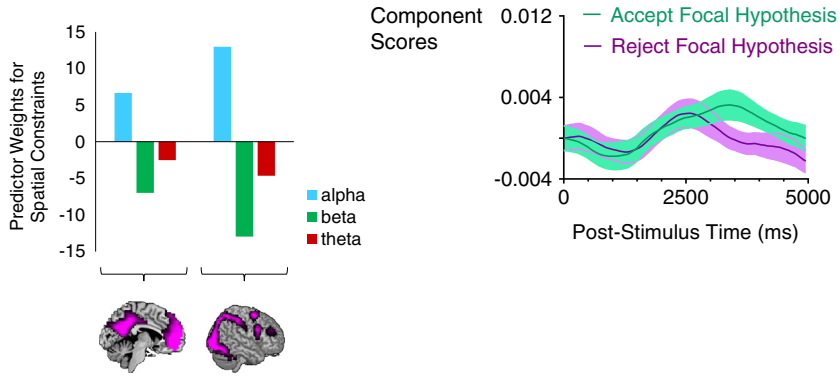

Fig. 8. Principal component 3 of the multimodal MEG–fMRI analysis, involving decreased beta-band power and increased alpha-band power in regions of both the default-mode network (DMN) and the fronto-parietal–occipital (FPO) network. In plots of the post-stimulus time courses of component scores, error bars (colors around trend lines in graphs at the right) represent the standard error of the mean. Brain images are from the previously published fMRI study and form the spatial constraints applied to the MEG data in the multimodal analysis. The intensity of the purple shading on those rendered brain images represents the strength of the fMRI component loadings (absolute value) for that voxel for that component.

have been shown to synchronize activity between frontal regions and more posterior regions, specifically temporal and parietal cortices (Doesburg et al., 2009b; Phillips et al., 2014; Salazar et al., 2012; Sauseng et al., 2005b; Varela et al., 2001). The temporal and spectral resolutions provided by MEG likely account for our ability to detect more functional networks than in an fMRI study in which participants performed the same task.

The use of MEG allowed us to distinguish between two networks involved in our hypothesis judgment task dominated by changes in alpha- and beta-band power. The first of these loaded most strongly onto visual areas (mostly parietal and lateral occipital cortices). Its time course did not differ significantly on the basis of whether the focal hypothesis was accepted. Instead, it is likely involved in the extensive amounts of visual scene processing common to both conditions in our task. The other network dominated by alpha- and beta-band activity loaded most strongly on the left DLPFC, VMPFC, PCC, and midline occipital cortex. It exhibited a stronger network signal in response to evidence–hypothesis matches, with the distinction between those two conditions being most evident in the beta frequency band.

It is interesting to speculate what these findings might mean for future studies involving more complex paradigms. The experimental paradigm used here was essentially a simplification of a paradigm used extensively in previous studies of probabilistic reasoning (Beach, 1968; Fischhoff and Beythmarom, 1983; Freeman et al., 2008; Hemsley and Garety, 1986; Moritz and Woodward, 2005; Speechley et al., 2010). In that paradigm, a series of beads was drawn from one of two jars, each of which contained a mixture of black and white beads. Each individual bead was drawn with replacement, and probability ratings could be compared to a Bayesian mathematical norm. If fMRI data were recorded during the performance of such a task, we might expect the strength of the signal from the underlying functional network to strengthen with each bead drawn, assuming that the series of beads involved the accumulation of evidence for one jar. More specifically, once a preferred jar emerged as the more likely source of the series of beads, that jar would correspond to the focal hypothesis. Each time a subsequent bead drawn matched the preferred or focal hypothesis, we would expect the strength of the signal from the underlying functionally connected network to increase.

We would also expect the brain regions forming that network to vary somewhat as a function of the specific nature of the hypothesis judgment task. For example, if the task involved a large visual display, as is the case in the study reported here, we would expect strong involvement of parietal and lateral occipital cortices. If the task involved monetary rewards or risks, we would expect involvement of dopaminergic regions such as the ventral tegmental area (Behrens et al., 2007). If the task involved motivations stemming from a sense of social identity, as in politically motivated reasoning, we might, in addition, expect involvement of the insula and orbitofrontal cortex, as well as the ventromedial–prefrontal and posterior cingulate cortices (Westen et al., 2006). It should be noted that coherence with pre-existing biases stored in long-term memory, such as those related to socio-political identities, could easily involve different networks (or groups of networks) than would coherence between novel items of information presented visually and processed only in short-term memory, as in the current study. The effects of coherence with social identity, however, could be studied in future research in a paradigm not reliant on knowledge stored in long-term memory. Instead, we could use a variant of the current task, manipulating whether the focal hypothesis was selected by the computer, by the participant, or by a fictional other participant from either the same social group or a different social group. That paradigm has already been used to establish a behavioral bias in favor of self-selected focal hypothesis (Whitman and Woodward, 2012), which is exacerbated in severely delusional schizophrenia patients (Whitman et al., 2012).

The results of the work reported here inform our interpretation of the cognitive aspects of hypothesis judgment. In the brain, evidence–hypothesis matches and mismatches are not simply opposite extremes of a continuous process. Rather, an evidence–hypothesis match that leads to hypothesis acceptance involves the formation of a coherent pattern in underlying neural networks. An evidence–hypothesis mismatch that should lead to hypothesis rejection involves only the lack of a pattern. This provides a potential neural mechanism for the many cognitive biases observed in human hypothesis judgment, such as confirmation bias in evidence gathering (Adsit and London, 1997; Gale and Ball, 2006; Klayman and Ha, 1987; Sanbonmatsu et al., 1998; Wason, 1960) and bias against disconfirmatory evidence (Buchy et al., 2007; Woodward et al., 2007). These can be explained by the fact that processing evidence supporting the hypothesis under consideration is naturally supported by the brain's basic mechanisms for linking information. Such information would be processed more fluidly and automatically than evidence refuting a hypothesis.

Blink and eye movement correction

We wished to remove blinks and eye movements from the ongoing MEG data using regression. While this was more computationally intensive than the more commonly used ICA (independent component analysis) approach for removing ocular artifacts, it allowed us to avoid any uncertainty as to whether a component reflected ocular artifacts or cortical processing, as it was more data-driven. This required a calibration task, as in previously published work using regression to remove ocular artifacts (Croft et al., 2005).

In our blink and eye movement calibration task, participants were asked to track a four-square black and white checkerboard as it moved unpredictably between the centers of the three lakes (all empty of fish), and to blink once each time the checkerboard turned green. There were 48 of these green blink instruction stimuli. For each of the possible three starting locations for the checkerboard there were 30 events in which it moved to each of the other two lakes. The stimulus onset asynchrony between these events varied randomly between 800 ms and 1600 ms. After every ten events, a red square was presented for 4 s. During these 4 s rest periods, the participants were free to blink as much or as little as desired.

In producing subject-specific estimates of the response at the MEG sensors associated with blinks (48 trials) and with each of the six types of saccades possible between the three lakes (30 trials each), we first determined the delay between the instruction to make a given blink or saccade and its occurrence. Within a given time window corresponding to a single artifact calibration event, we identified the peaks of blinks as time points with maximal z-scores. We identified the mid-points of saccades, characterized by steep slopes, as brief time-windows with high standard deviations. Both of these methods are described in more detail below. This search for the peaks of blinks and the mid-points of saccades allowed us to average across the 48 blink events by temporally aligning their peaks, and to average across the 30 occurrences of each type of saccade by temporally aligning their mid-points.

In order to identify these temporal mid-points, we selected individual channels on which blinks (MLT41) and saccades (LF11) were clearly visible in all participants. To find the peak of each type of blink, we converted the 1400 samples following the instruction to make a blink into absolute values of z-scores. We removed any brief spikes of very high-frequency noise from the z-score time courses by temporally smoothing the 1400-sample vector. Specifically, we averaged sets of 120 adjacent samples, with this smoothing window shifting in one-sample increments. The largest absolute value z-score in this smoothed vector was taken to be at the mid-point (the peak) of the blink.

In identifying when saccades occurred, we took a 1400-sample segment, and searched for the 50-sample window (using one-sample sliding increments) with the largest standard deviation. This allowed us to find the mid-point of the steep slope characterizing a saccade. Once these mid-points were identified for each requested blink and saccade, we used them to temporally align these events and produce

150-channel subject-specific artifact averages for blinks and for each of the six types of saccade. These artifact averages were 1000 samples long for blinks and 400 samples long for saccades, centered at the mid-point of the artifact.

We then searched the ongoing data from the probabilistic reasoning task, using sliding windows with data segments of either 400 or 1000 samples, to regress each brief data segment onto each artifact average. For each artifact type and each run of the probabilistic reasoning task, this produced a 16 min time series of beta weights indicating how closely the data surrounding each sample resembled the average for that type of artifact. These artifact-specific beta time series produced a seven-column model (one column for blinks, and six for the six types of saccades) onto which the full 150-channel dataset for each 16 min run could be regressed. The variance predictable from the seven-column artifact model (the matrix of predicted scores) was subtracted out. The remaining portion of variance (the matrix of residuals) was used as the artifact-free data in all subsequent stages of analysis. All of these computations were done using Matlab software. The chosen sizes of arbitrary time windows for smoothing or for the calculations of standard deviations were based on visual inspection of the plotted time courses of individual artifacts.

Funding

This research was funded by a Natural Sciences and Engineering Research Council of Canada Operating Grant (RGPIN 343016–07), a Canadian Institutes of Health Research New Investigator Award (T.S.W.), a Michael Smith Foundation for Health Research Scholar Award (T.S.W.), a Natural Sciences and Engineering Research Council of Canada Post Graduate Scholarship Award (J.C.W.), and a Michael Smith Foundation for Health Research Senior Trainee Award (J.C.W.).

Acknowledgments

We would like to thank Jen Riley and Jessica Ferguson-King for assistance with data collection and data management and John Paiement for assistance with software development. We also thank the staff of the MEG facility at the Down Syndrome Research Foundation and the staff of the UBC 3T MRI Research Centre for their support during data collection. We thank the WestGrid subdivision of the Compute Canada Consortium for providing the high-performance computing resources used.

References

Adsit, D.J., London, M., 1997. Effects of hypothesis generation on hypothesis testing in rule-discovery tasks. J. Gen. Psychol. 124 (1), 19–34.

Beach, L.R., 1968. Probability magnitudes and conservative revision of subjective probabilities. J. Exp. Psychol. 77 (1), 57–63.

Behrens, T.E.J., Woolrich, M.W., Walton, M.E., Rushworth, M.F.S., 2007. Learning the value of information in an uncertain world. Nat. Neurosci. 10 (9), 1214–1221. http://dx.doi.org/10.1038/Nn1954.

Belluscio, M.A., Mizuseki, K., Schmidt, R., Kempter, R., Buzsaki, G., 2012. Cross-frequency phase–phase coupling between theta and gamma oscillations in the hippocampus. J. Neurosci. 32 (2), 423–435. http://dx.doi.org/10.1523/JNEUROSCI.4122-11.2012.

Buchy, L., Woodward, T.S., Liotti, M., 2007. A cognitive bias against disconfirmatory evidence (BADE) is associated with schizotypy. Schizophr. Res. 90 (1–3), 334–337. http://dx.doi.org/10.1016/j.schres.2006.11.012.

Buckner, R.L., Andrews-Hanna, J.R., Schacter, D.L., 2008. The brain's default network — anatomy, function, and relevance to disease. Ann. N. Y. Acad. Sci. 1124, 1–38. http://dx.doi.org/10.1196/annals.1440.011.

Christoff, K., Gordon, A.M., Smallwood, J., Smith, R., Schooler, J.W., 2009. Experience sampling during fMRI reveals default network and executive system contributions to mind wandering. Proc. Natl. Acad. Sci. U. S. A. 106 (21), 8719–8724. http://dx.doi.org/10.1073/pnas.0900234106.

Colgin, L.L., Denninger, T., Fyhn, M., Hafting, T., Bonnevie, T., Jensen, O., ... Moser, E.I., 2009. Frequency of gamma oscillations routes flow of information in the hippocampus. Nature 462 (7271) 353-U119. doi: 10.1038/Nature08573.

Croft, R.J., Chandler, J.S., Barry, R.J., Cooper, N.R., Clarke, A.R., 2005. EOG correction: a comparison of four methods. Psychophysiology 42 (1), 16–24. http://dx.doi.org/10.1111/j.1469–8986.2005.00264.x.

Delorme, A., Makeig, S., 2004. EEGLAB: an open source toolbox for analysis of single-trial EEG dynamics including independent component analysis. J. Neurosci. Methods 134 (1), 9–21. http://dx.doi.org/10.1016/j.jneumeth.2003.10.009.

Doesburg, S.M., Green, J.J., McDonald, J.J., Ward, L.M., 2009a. From local inhibition to long-range integration: a functional dissociation of alpha-band synchronization across cortical scales in visuospatial attention. Brain Res. 1303, 97–110. http://dx.doi.org/10.1016/j.brainres.2009.09.069.

Doesburg, S.M., Green, J.J., McDonald, J.J., Ward, L.M., 2009b. Rhythms of consciousness: binocular rivalry reveals large-scale oscillatory network dynamics mediating visual perception. PLoS One 4 (7), 1–14. http://dx.doi.org/10.1371/Journal.Pone.0006142.

Donner, T.H., Siegel, M., Fries, P., Engel, A.K., 2009. Buildup of choice-predictive activity in human motor cortex during perceptual decision making. Curr. Biol. 19 (18), 1581–1585.

Engel, A.K., Fries, P., 2010. Beta-band oscillations—signalling the status quo? Curr. Opin. Neurobiol. 20 (2), 156–165. http://dx.doi.org/10.1016/j.conb.2010.02.015.

Fischhoff, B., Beythmarom, R., 1983. Hypothesis evaluation from a Bayesian perspective. Psychol. Rev. 90 (3), 239–260.

Fox, M.D., Snyder, A.Z., Vincent, J.L., Corbetta, M., Van Essen, D.C., Raichle, M.E., 2005. The human brain is intrinsically organized into dynamic, anticorrelated functional networks. Proc. Natl. Acad. Sci. 102 (27), 9673–9678. http://dx.doi.org/10.1073/pnas.0504136102.

Fox, M.D., Zhang, D.Y., Snyder, A.Z., Raichle, M.E., 2009. The global signal and observed anticorrelated resting state brain networks. J. Neurophysiol. 101 (6), 3270–3283. http://dx.doi.org/10.1152/jn.90777.2008.

Freeman, D., Pugh, K., Garety, P., 2008. Jumping to conclusions and paranoid ideation in the general population. Schizophr. Res. 102 (1–3), 254–260. http://dx.doi.org/10.1016/j.schres.2008.03.020 S0920-9964(08)00162-X [pii].

Gale, M., Ball, L.J., 2006. Dual-goal facilitation in Wason's 2–4–6 task: what mediates successful rule discovery? Q. J. Exp. Psychol. 59 (5), 873–885 doi: 10.1080/02724980543000051.

Gross, J., Kujala, J., Hamalainen, M., Timmermann, L., Schnitzler, A., Salmelin, R., 2001. Dynamic imaging of coherent sources: studying neural interactions in the human brain. Proc. Natl. Acad. Sci. U. S. A. 98 (2), 694–699.

Haxby, J.V., 2012. Multivariate pattern analysis of fMRI: the early beginnings. NeuroImage 62 (2), 852–855.

Heekeren, H.R., Marrett, S., Bandettini, P.A., Ungerleider, L.G., 2004. A general mechanism for perceptual decision-making in the human brain. Nature 431 (7010), 859–862. http://dx.doi.org/10.1038/Nature02966.

Heekeren, H.R., Marrett, S., Ruff, D.A., Bandettini, P.A., Ungerleider, L.G., 2006. Involvement of human left dorsolateral prefrontal cortex in perceptual decision making is independent of response modality. Proc. Natl. Acad. Sci. U. S. A. 103 (26), 10023–10028. http://dx.doi.org/10.1073/pnas.0603949103.

Hemsley, D.R., Garety, P.A., 1986. The formation of maintenance of delusions — a Bayesian analysis. Br. J. Psychiatry 149, 51–56.

Herdman, A.T., Cheyne, D., 2009. A practical guide for MEG and beamforming. In: Handy, T.C. (Ed.), *Brain Signal Analysis: Advances in Neuroelectric and Neuromagnetic Methods*. MIT Press, Cambridge, Mass, pp. 99–140.

Hunter, M.A., Takane, Y., 2002. Constrained principal component analysis: various applications. J. Educ. Behav. Stat. 27 (2), 105–145.

Jolliffe, I.T., 1986. Principal Component Analysis. Springer, New York.

Kelly, S.P., Lalor, E.C., Reilly, R.B., Foxe, J.J., 2006. Increases in alpha oscillatory power reflect an active retinotopic mechanism for distracter suppression during sustained visuospatial attention. J. Neurophysiol. 95 (6), 3844–3851.

Kim, J.N., Shadlen, M.N., 1999. Neural correlates of a decision in the dorsolateral prefrontal cortex of the macaque. Nat. Neurosci. 2 (2), 176–185.

Klayman, J., Ha, Y.W., 1987. Confirmation, disconfirmation, and information in hypothesis-testing. Psychol. Rev. 94 (2), 211–228.

Köhler, W., 1929. Gestalt Psychology. H. Liveright, New York.

Lavigne, K.M., Metzak, P.D., Woodward, T.S., 2015. Functional brain networks underlying detection and integration of disconfirmatory evidence. NeuroImage 112, 138–151.

Metzger, W., 2006. Laws of Seeing. MIT Press, Cambridge, Mass.

Moritz, S., Woodward, T.S., 2005. Jumping to conclusions in delusional and non-delusional schizophrenic patients. Br. J. Clin. Psychol. 44, 193–207 doi: 10.1348/014466505 × 35678.

Nickerson, R.S., 1998. Confirmation bias: a ubiquitous phenomenon in many guises. Rev. Gen. Psychol. 2 (2).

Oostenveld, R., Fries, P., Maris, E., Schoffelen, J.M., 2011. FieldTrip: open source software for advanced analysis of MEG, EEG, and invasive electrophysiological data. Comput. Intell. Neurosci. http://dx.doi.org/10.1155/2011/156869.

Pfurtscheller, G., Stancak Jr., A., Neuper, C., 1996. Post-movement beta synchronization. A correlate of an idling motor area? Electromyogr. Clin. Neurophysiol. 98 (4), 281–293.

Pfurtscheller, G., Woertz, M., Supp, G., Lopes da Silva, F.H., 2003. Early onset of post-movement beta electroencephalogram synchronization in the supplementary motor area during self-paced finger movement in man. Neurosci. Lett. 339 (2), 111–114.

Phillips, J.M., Vinck, M., Everling, S., Womelsdorf, T., 2014. A long-range fronto-parietal 5- to 10-Hz network predicts "top–down" controlled guidance in a task-switch paradigm. Cereb. Cortex 24 (8), 1996–2008.

Rihs, T.A., Michel, C.M., Thut, G., 2007. Mechanisms of selective inhibition in visual spatial attention are indexed by alpha-band EEG synchronization. Eur. J. Neurosci. 25 (2), 603–610.

Salazar, R.F., Dotson, N.M., Bressler, S.L., Gray, C.M., 2012. Content-specific fronto-parietal synchronization during visual working memory. Science 338 (6110), 1097–1100.

Sanbonmatsu, D.M., Posavac, S.S., Kardes, F.R., Mantel, S.P., 1998. Selective hypothesis testing. *Psychon. Bull. Rev.* 5 (2), 197–220.

Sauseng, P., Klimesch, W., Stadler, W., Schabus, M., Doppelmayr, M., Hanslmayr, S., ... Birbaumer, N., 2005a. A shift of visual spatial attention is selectively associated with human EEG alpha activity. Eur. J. Neurosci. 22 (11), 2917–2926.

Sauseng, P., Klimesch, W., Schabus, M., Doppelmayr, M., 2005b. Fronto-parietal EEG coherence in theta and upper alpha reflect central executive functions of working memory. Int. J. Psychophysiol. 57 (2), 97–103.
Sauseng, P., Griesmayr, B., Freunberger, R., Klimesch, W., 2010. Control mechanisms in working memory: a possible function of EEG theta oscillations. Neurosci. Biobehav. Rev. 34 (7), 1015–1022.
Schack, B., Klimesch, W., Sauseng, P., 2005. Phase synchronization between theta and upper alpha oscillations in a working memory task. Int. J. Psychophysiol. 57 (2), 105–114.
Sheth, B.R., Sandkuhler, S., Bhattacharya, J., 2009. Posterior beta and anterior gamma oscillations predict cognitive insight. J. Cogn. Neurosci. 21 (7), 1269–1279.
Siegel, M., Engel, A.K., Donner, T.H., 2011. Cortical network dynamics of perceptual decision-making in the human brain. Front. Hum. Neurosci. 5.
Speechley, W.J., Whitman, J.C., Woodward, T.S., 2010. The contribution of hypersalience to the "jumping to conclusions" bias associated with delusions in schizophrenia. J. Psychiatry Neurosci. 35 (1), 7–17. http://dx.doi.org/10.1503/Jpn.090025.
Varela, F., Lachaux, J.P., Rodriguez, E., Martinerie, J., 2001. The brainweb: phase synchronization and large-scale integration. Nat. Rev. Neurosci. 2 (4), 229–239.
Wason, P.C., 1960. On the failure to eliminate hypotheses in a conceptual task. Q. J. Exp. Psychol. 12 (3), 129–140.
Westen, D., Blagov, P.S., Harenski, K., Kilts, C., Hamann, S., 2006. Neural bases of motivated reasoning: an fMRI study of emotional constraints on partisan political judgment in the 2004 US presidential election. J. Cogn. Neurosci. 18 (11), 1947–1958.
Whitman, J.C., Woodward, T.S., 2012. Self-selection bias in hypothesis comparison. Organ. Behav. Hum. Decis. Process. 118 (2), 216–225.
Whitman, J.C., Menon, M., Kuo, S.S., Woodward, T.S., 2012. Bias in favour of self-selected hypotheses is associated with delusion severity in schizophrenia. Cogn. Neuropsychiatry 18 (5), 376–389. http://dx.doi.org/10.1080/13546805.2012.715084.
Whitman, J.C., Metzak, P.D., Lavigne, K.M., Woodward, T.S., 2013a. Functional connectivity in a frontoparietal network involving the dorsal anterior cingulate cortex underlies decisions to accept a hypothesis. Neuropsychologia 51, 1132–1141.
Whitman, J.C., Ward, L.M., Woodward, T.S., 2013b. Patterns of cortical oscillations organize neural activity into whole-brain functional networks evident in the fMRI BOLD signal. Front. Hum. Neurosci. 7.
Woodward, T.S., Buchy, L., Moritz, S., Liotti, M., 2007. A bias against disconfirmatory evidence is associated with delusion proneness in a nonclinical sample. Schizophr. Bull. 33 (4), 1023–1028. http://dx.doi.org/10.1093/schbul/sbm013.
Worden, M.S., Foxe, J.J., Wang, N., Simpson, G.V., 2000. Anticipatory biasing of visuospatial attention indexed by retinotopically specific alpha-band electroencephalography increases over occipital cortex. J. Neurosci. 20 (6) art. no.-RC63.
Wu, X., Chen, X.C., Li, Z.H., Han, S.H., Zhang, D., 2007. Binding of verbal and spatial information in human working memory involves large-scale neural synchronization at theta frequency. NeuroImage 35 (4), 1654–1662.
Yeo, B.T.T., Krienen, F.M., Sepulcre, J., Sabuncu, M.R., Lashkari, D., Hollinshead, M., ... Buckner, R.L., 2011. The organization of the human cerebral cortex estimated by intrinsic functional connectivity. J. Neurophysiol. 106 (3), 1125–1165.